Electronic Supplementary Material (ESI) for Chemical Communications.
This journal is © The Royal Society of Chemistry 2024

Electron-insulating Li_2O protection layer endowing Li-Cu-Zn ternary alloy composite anode with high performance

Linyun Yi[a,b], Zihao Wang[a,b], Jianxiong Xing[a,b], Xiaoxiao Chen[a,b], Hao Huang[a,b], Chaohui Wei[b], Qiang Zhao[a,b], Aijun Zhou[a,b], Jingze Li[a,b]*

a School of Materials and Energy, University of Electronic Science and Technology of China, Chengdu 611731, P. R. China

b Huzhou Key Laboratory of Smart and Clean Energy, Yangtze Delta Region Institute (Huzhou), University of Electronic Science and Technology of China, Huzhou 313001, P. R. China

Corresponding author E-mail: lijingze@uestc.edu.cn (J. Z. Li)

Experimental section

Preparations of LCZO electrodes

All of the preparation processes were conducted in an Ar-filled glovebox with O_2 and H_2O content below 0.1 ppm. 0.5 g Li, 0.08 g Cu, and 0.17 g ZnO powder were mixed and melted evenly at 400 ℃ (Fig. 1a). LZ electrode only contains Li metal (0.5 g) and Zn metal (0.12 g). LZO electrode contains Li metal (0.5 g) and ZnO powder (0.17 g). As the temperature increased, Li metal gradually melted, during which vigorous stirring was applied to uniformly disperse the ZnO powder into the liquid Li metal. When the white ZnO powder (Fig. S1, ESI) completely reacted with Li metal, the uniform molten Li composite was coated on the stainless steel foil. After cooling down to room temperature, LCZO composites anode with different mass ratios were given (the atomic ratio of Li, Cu and Zn is 60: 1: 1, 60: 1: 2 and 60: 1: 3, respectively). The performance of LCZO composite anode increases with the increment of ZnO content, but at the expense of capacity loss (Fig. S11, ESI). Therefore, the atomic ratio of Li, Cu and Zn is 60: 1: 2 in all tests in this work.

Characterizations

X-ray diffraction (XRD) was tested using Cu Kα (λ = 0.154 nm) radiation over 2θ range from 10° to 80° at 10° min^{-1}. To prevent oxidation of the samples during testing, we utilized polyimide tape to seal the samples. Scanning electron microscope (SEM) and energy dispersive X-ray spectroscopy (EDS) (FE-SEM, Hitachi, S3400N) analysis of electrode morphology was characterized at 15 kV. The Fourier transform infrared (FTIR) (Bruker, Vertex80V) was used to detect the components of the LCZO electrode with the wave number range from 400 to 4000 cm^{-1}. Raman spectra were taken in a micro Raman spectroscopy (HORIBA, XploRA PLUS) with the shift number range from 100 to 4000 cm^{-1}.

Electrochemical measurements

All galvanostatic electrochemical tests were done on a Neware battery testing system at a constant temperature of 25 ℃. Electrochemical impedance spectroscopy (EIS) was tested on an electrochemical workstation (CHI660C, Shanghai, Chenhua) in the frequency range of 1 MHz to 100 mHz with a perturbation voltage amplitude of 5 mV. The electrochemical performance of the LCZO anode was tested by assembling a symmetrical cell in a standard CR2032 coin cell. The electrolyte was 1 M lithium hexafluorophosphate ($LiPF_6$) in ethylene carbonate/diethyl carbonate (EC/DEC) (1:1 by volume) with 5% fluoroethylene carbonate (FEC) and 1 M LiTFSI and 2% $LiNO_3$ dissolved in 1,3-dioxolane (DOL) and 1,2-dimethoxyethane (DME) (1:1 by volume). All symmetrical cells were added with 120 μL of electrolyte and equipped with Celgard 2325 membrane as the separator.

For the full cell test, the LFP cathode was paired with the LCZO composite anode or Li metal anode. The active material LFP powder, super P and polyvinylidene fluoride (PVDF) (8:1:1, w/w) were mixed in N-methyl-2-pyrrolidone (NMP) to form a uniform slurry, which was posted on an Al foil. The areal loadings of LFP were about 11.5 mg cm^{-2} (1.7 mAh cm^{-2}) and 17.2 mg cm^{-2} (2.45 mAh cm^{-2}), seperately. The electrolyte was 1.0 M $LiPF_6$ in EC/DEC (1:1, v/v) with 5% FEC and the electrolyte used was fixed at 120 μL. The full cells were cycled between 2.5 and 4.2 V at different current densities.

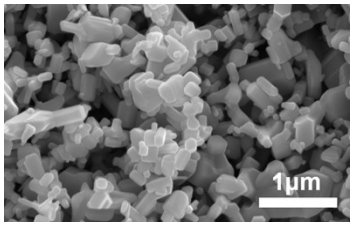

Fig. S1. The SEM image of ZnO powders.

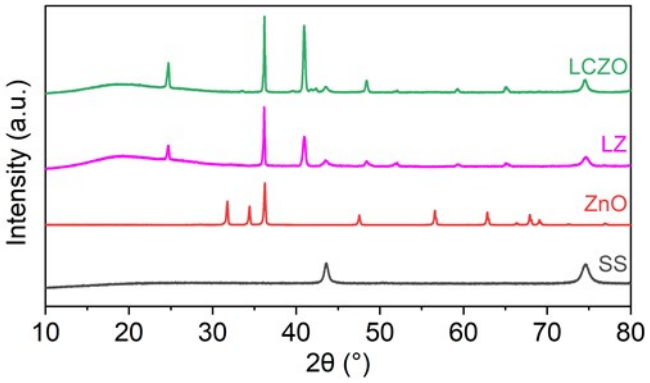

Fig. S2. The XRD patterns of LCZO, LZ, ZnO and SS.

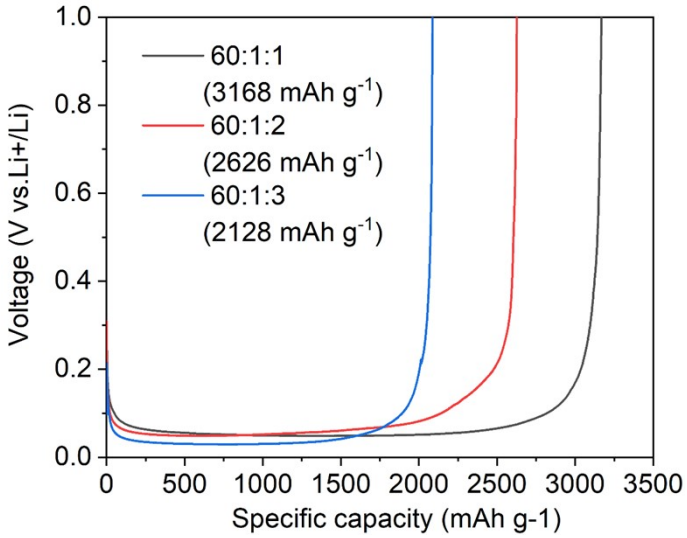

Fig. S3. The delivered specific capacity of LCZO electrode after stripping Li to 1 V vs Li^+/Li.

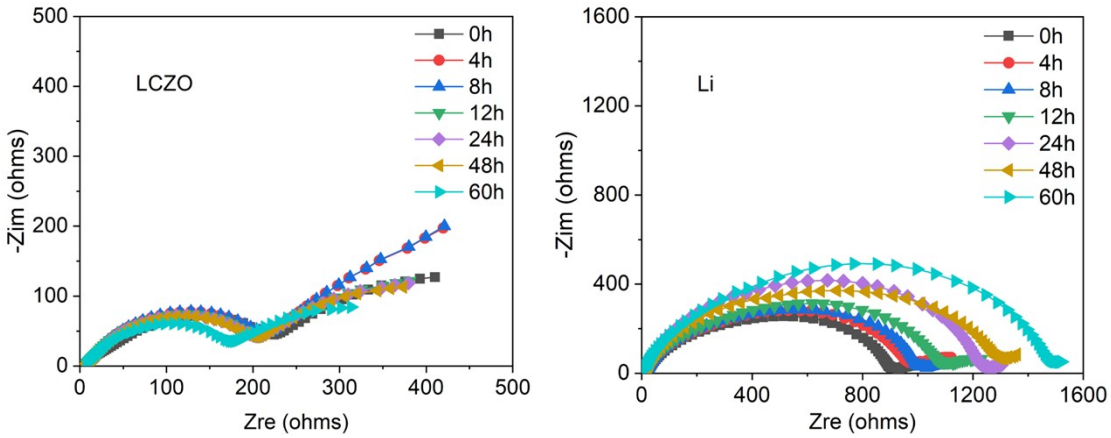

(a) (b)

Fig. S4 EIS spectra of different symmetric Li cells with carbonate electrolyte after different rest time before cycling. (a) Pure Li metal electrode. (b) LCZO electrode.

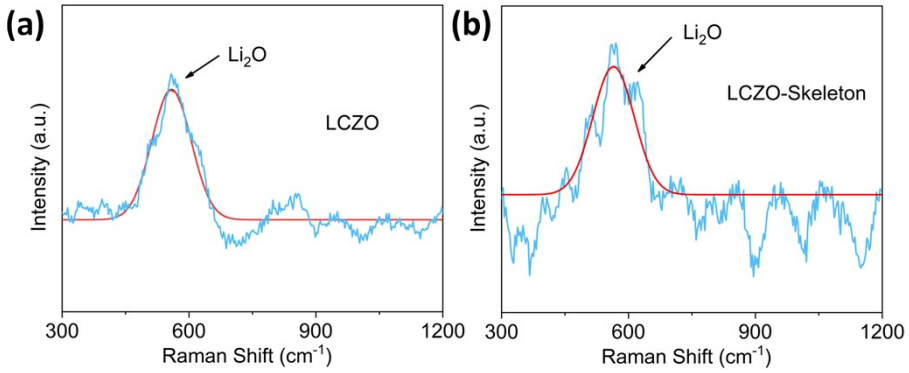

Fig. S5. (a, b) Raman spectra of the LCZO electrode and the delithiated LCZO, separately.

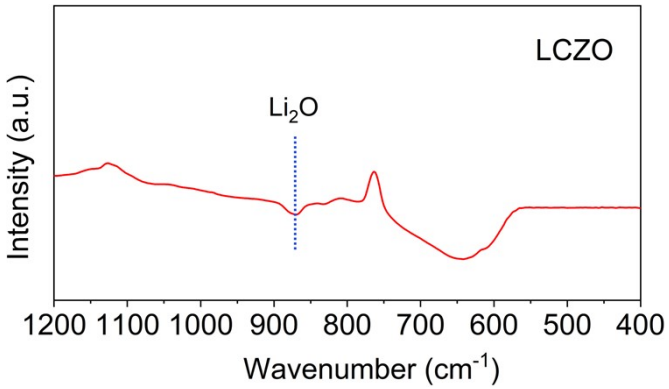

Fig. S6. The FTIR spectrum of the pristine LCZO.

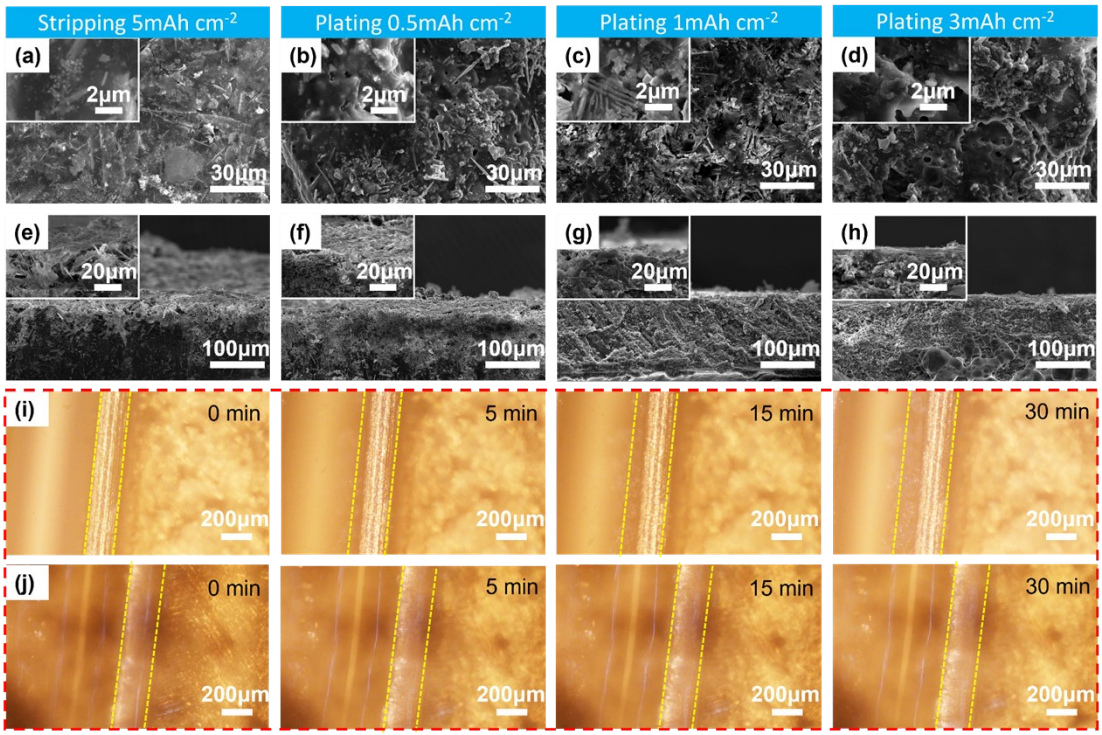

Fig. S7. (a) Top-view SEM images of the LCZO electrode after pre-stripping a capacity of 5 mAh cm^{-2}. Top-view SEM images of the LCZO electrode with Li deposition at different capacities: (b) 0.5 mAh cm^{-2}, (c) 1 mAh cm^{-2}, (c) 3 mAh cm^{-2}. (e-h) and the corresponding side-view SEM images of Li deposition, respectively. (i, j) *in-situ* optical microscope images of Li and LCZO electrodes at the plating time of 0-30 min with 5 mA cm^{-2}.

To evaluate the electrochemical performance, LCZO/LCZO symmetric cells were tested with various areal capacities at 1 mA cm^{-2}. As a reference, Li/Li symmetric cells were assembled. Figs. S7a and e (ESI) show top-view and side-view SEM images of LCZO with a delithiated capacity of 5 mA h cm^{-2}. Fig. S7b–d (ESI) show SEM images of the LCZO electrode with Li deposition to different capacities. When the deposition of Li increases to 0.5 mA h cm^{-2}, a small amount of Li fills inside the alloy skeleton, and no Li dendrite growth is observed on the surface. When the deposition of Li increases to 1 mA h cm^{-2}, Li^+ ions continue to pass through the artificial SEI layer constructed by Li_2O to fill pores inside the skeleton, realizing a dense deposition of Li. A large amount of Li_2O forms a stable interface to regulate the transport of Li ions, so that Li is uniformly deposited within the Li–Cu–Zn ternary alloy framework.[1] As the deposition of Li further increases

to 3 mA h cm^{-2}, Li gradually fills the gaps of the alloy skeleton. In distinctive contrast, obvious cracks and dendrites can be observed on the bare Li surface, which is regarded as the reason for battery failure (Fig. S8, ESI). In situ optical microscopy was used to monitor the deposition behavior of Li plating at 5 mA cm^{-2} (Fig. S7i and j, ESI). In the bare Li electrode, uneven protrusions appear on the surface of Li after electroplating for 15 min, which continue to grow with time (Fig. S7i, ESI). Inversely, in the case of the LCZO electrode, Li deposited uniformly inside the alloy skeleton (Fig. S7j, ESI). No dendrites or dead Li were observed within 30 min, indicating that the alloy skeleton plays an important role in inducing deposition and controlling nucleation sites.

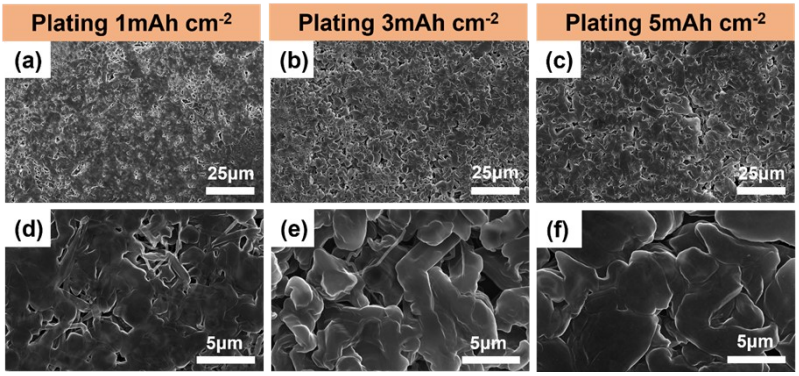

Fig. S8. The top-view SEM images of the bare Li electrodes after Li plating for (a) 1 mAh cm^{-2}, (c) 3 mAh cm^{-2}, (e) 5 mAh cm^{-2}, respectively. (b, d and f) The corresponding enlarged SEM images of the LCZO electrodes after Li plating, respectively. The current density is 1 mA cm^{-2}.

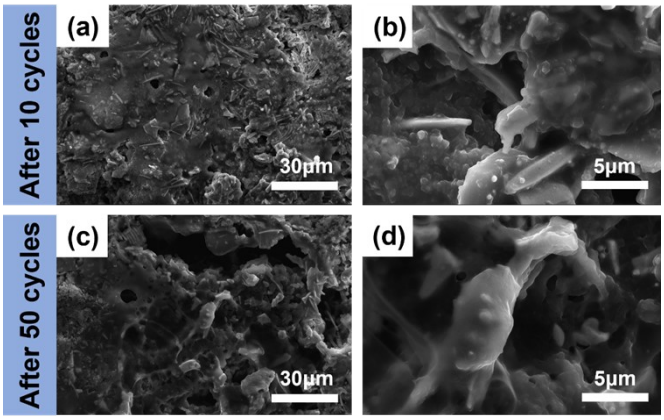

Fig. S9. (a, b) Top-view SEM images of the LCZO electrodes after 10 symmetric cycles under 1 mA cm^{-2} and 1 mAh cm^{-2}. (c, d) Top-view SEM images of the LCZO electrodes after 50 symmetric cycles under 1 mA cm^{-2} and 1 mAh cm^{-2}.

To compare the morphologies of the bare Li anode and LCZO anode, we conducted SEM characterization after cycling the two cells for 10 cycles and 50 cycles at 1 mA cm^{-2} and 1 mA h cm^{-2}, separately. The surface of the LCZO anode (Fig. S9, ESI) maintains a dense morphology without any traces of dendritic Li. The stable SEI layer constructed by Li_2O induces uniform transport of Li^+ ions and further cooperates with the alloy frame below to achieve uniform and dense deposition. This improved morphology is also observed over prolonged cycling periods, indicating that the LCZO anode sustains a uniform structure and inhibits Li dendrite formation throughout continuous cycling. To further corroborate the structural stability of the LCZO anode, a long-term cycling test was carried out. In contrast to the extensively distorted bare Li surface, which exhibits severe Li dendrite growth and a significant volume shift (Fig. S10, ESI), the surface of the LCZO anode remains flat and dense with no protrusions or pulverization on the skeleton. This highlights the ability of the skeleton to withstand the internal stress caused by electrode volume changes during cycling. The presence of dendritic Li damages the fragile SEI, leading to the formation of a thick and porous layer of dead Li on the surface. However, the alloy skeleton in the composite anode allows Li metal to deposit inside the alloy network frame, preventing direct deposition on the

surface. The skeleton framework effectively restricts Li metal deposition, curtails Li dendrites growth, and mitigates electrode volume change during cycling.

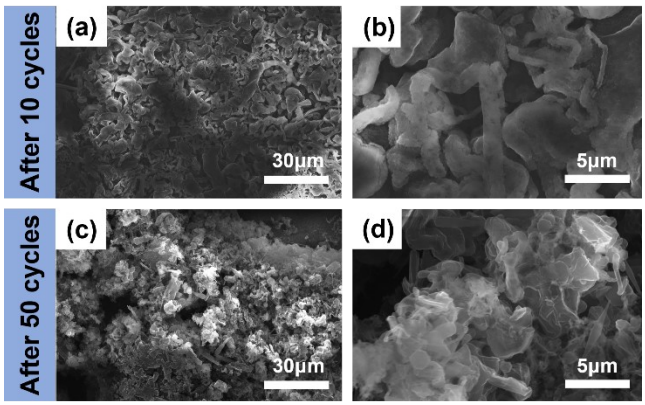

Fig. S10. (a, b) Top-view SEM images of the bare Li electrodes after 10 symmetric cycles under 1 mA cm^{-2} and 1 mAh cm^{-2}. (c, d) Top-view SEM images of the bare Li electrodes after 50 symmetric cycles under 1 mA cm^{-2} and 1 mAh cm^{-2}.

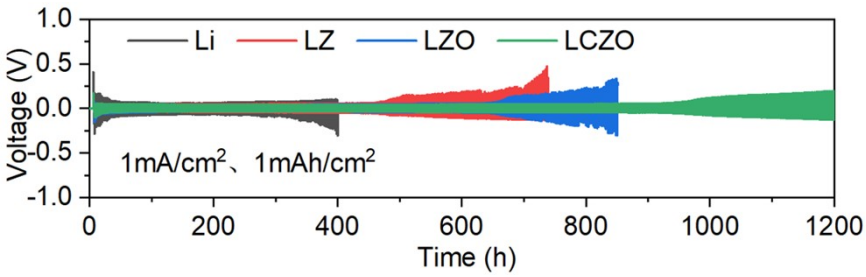

Fig. S11 Galvanostatic cycling diagrams of the symmetric cells tested at 1 mA cm^{-2} for a capacity of 1 mAh cm^{-2}.

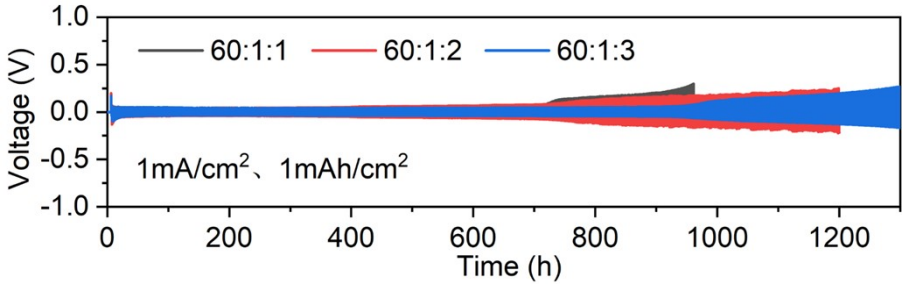

Fig. S12 Galvanostatic cycling diagrams of the symmetric cells of the LCZO electrodes with different atomic ratios of Li: Cu: Zn.

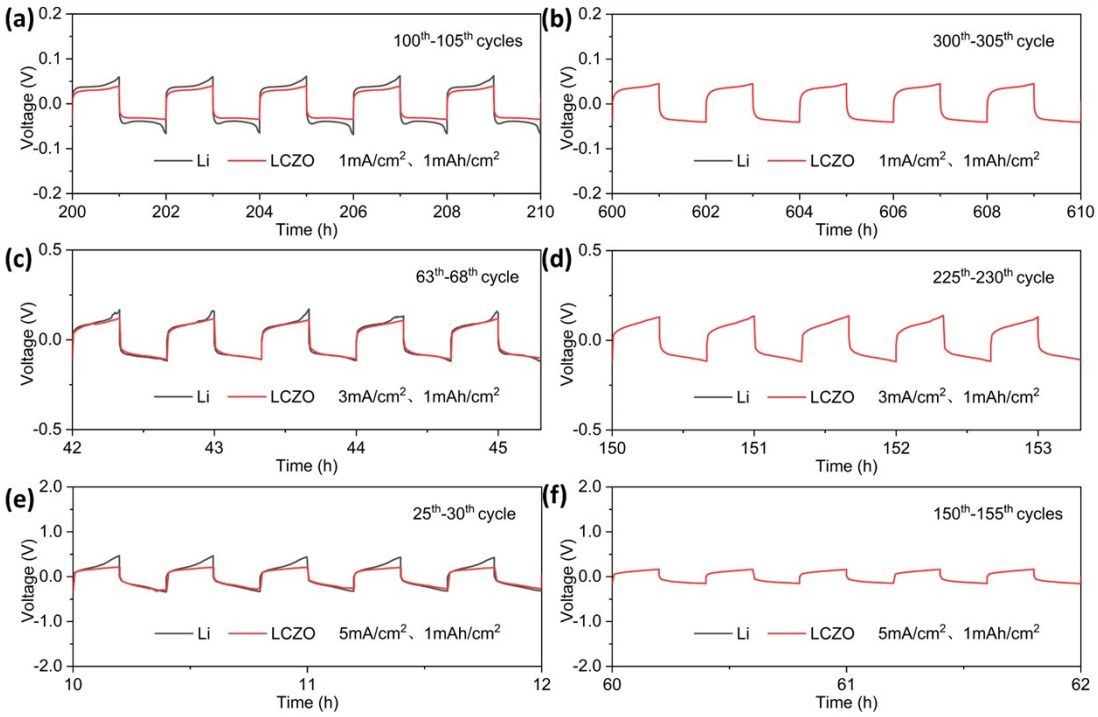

Fig. S13. Detailed voltage profiles of (a, b) 1 mA cm^{-2}, (c, d) 3 mA cm^{-2}, (e, f) 5 mA cm^{-2} with a fixed capacity of 1 mAh cm^{-2} at different cycles.

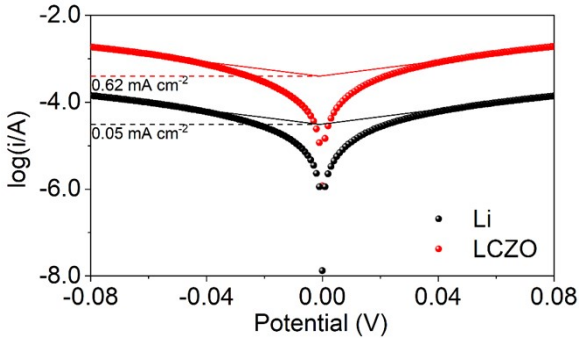

Fig. S14. Tafel plots of the bare Li|Li and LCZO|LCZO symmetric cells.

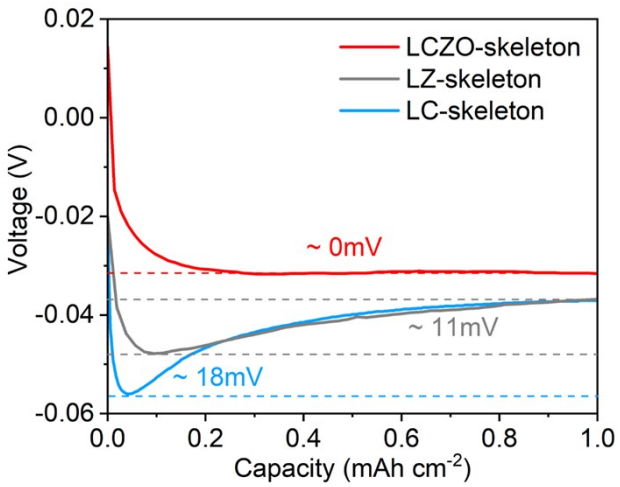

Fig. S15 The voltage-capacity curve of Li plating on the skeleton after electrochemical delithiated completely.

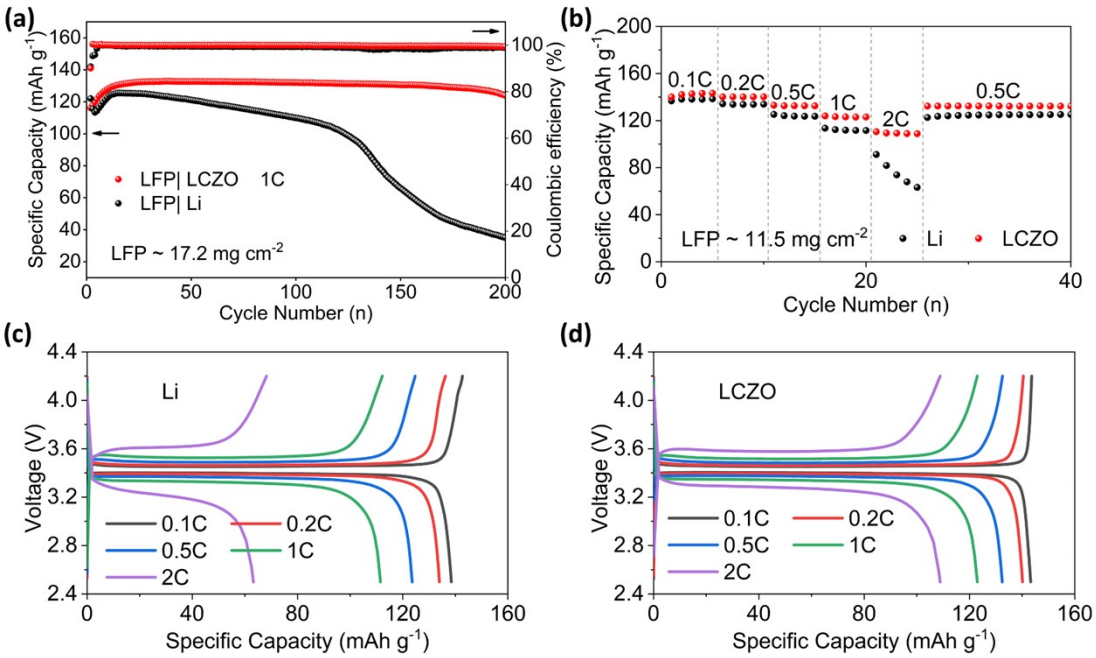

Fig. S16. (a) Cycling performance of the full cells with the LCZO and Li foil as the anode and LFP as the cathode tested at 1C with high areal capacity of 2.45 mAh cm^{-2}. (b) Rate performances of the full cells with two styles of anodes. Voltage profiles of the full cells using (c) LCZO and (d) bare Li as the anode at various rates from 0.1C to 2C.

Table S1 Comparison of the LCZO composite anode in this work with other Li-rich alloys reported in recent publications.

Materials	Electrolyte Components	Current density (mA cm^{-2})	Capacity (mAh cm^{-2})	Cycle Life (h)	References
Zn/ZnO@Li	1M LiTFSI in DOL/DME with 1% $LiNO_3$	0.5 4	1 1	900 500	J. Mater. Chem.A, 2019, 7, 11683-11689.[2]
CuLi60	1M LiTFSI in DOL/DME with 2% $LiNO_3$	1	1	1400	Science Bulletin, 2020, 65, 1907-1915.[3]
AlLi20	1 M $LiPF_6$ in EC/DEC with 5% FEC	1 3	1 1	1400 300	J. Alloys Compd., 2023, 960.[4]
ZnLi10	1M LiTFSI in DOL/DME with 2% $LiNO_3$	1	1	2800	Journal of Energy Chemistry, 2020, 51, 285-292.[5]
LiMg/Li_3PO_4	1M LiTFSI in DOL/DME with 2% $LiNO_3$	1	1	1000	Chemical Engineering Journal, 2022, 439.[6]
Li/MgO/S@PAN	1 M $LiPF_6$ in EC/DMC with 10% FEC	1 2	1 4	900 600	Energy Storage Materials, 2020, 33, 452-459.[7]
Li/PVDF/PMMA/ZnO	1 M $LiPF_6$ in EC/DMC with 10% FEC	1 1 4	1 8 4	1000 800 150	Nano Energy, 2022, 95.[8]
Li/SiO_2	1M LiTFSI in DOL/DME	1	3	700	Adv. Mater., 2019, 31, e1807585.[9]
Li-B-Mg	1 M $LiPF_6$ in EC/EMC/DMC with VC	0.5 1 2	0.5 0.5 0.5	500 350 150	Adv. Sci., 2020, 7, 1902643.[10]
Li_2Cu_3Zn	1M LiTFSI in DOL/DME with 1% $LiNO_3$	1 2 4	1 2 4	1200 800 400	J. Alloys Compd., 2022, 926, 166437.[11]
LCZO	1 M $LiPF_6$ in EC/DEC with 5% FEC	1 3 5	1 1 1	1200 300 150	This work

Reference

1. X.-X. Ma, X. Shen, X. Chen, Z.-H. Fu, N. Yao, R. Zhang and Q. Zhang, *Small Structures*, 2022, **3**.

2. Q. Chen, Y. Yang, H. Zheng, Q. Xie, X. Yan, Y. Ma, L. Wang and D.-L. Peng, *J. Mater. Chem.A*, 2019, **7**, 11683-11689.
3. W. Jia, Y. Liu, Z. Wang, F. Qing, J. Li, Y. Wang, R. Xiao, A. Zhou, G. Li, X. Yu, Y.-S. Hu, H. Li, Z. Wang, X. Huang and L. Chen, *Science Bulletin*, 2020, **65**, 1907-1915.
4. C. Wei, J. Ruan, Z. Song, X. Chen, D. Wang, J. Jiang, X. Wang, A. Zhou, W. Zou and J. Li, *J. Alloys Compd.*, 2023, **960**.
5. Z. Yao, W. Jia, Z. Wang, J. Ruan, X. Kong, X. Guan, Z. Wang, J. Li, Y. Wang, W. Zou and F. Zhou, *Journal of Energy Chemistry*, 2020, **51**, 285-292.
6. K. Peng, Z. Chen, X. Zhao, K. Shi, C. Zhu and X. Yan, *Chemical Engineering Journal*, 2022, **439**.
7. H. Lu, T. Zhang, Y. Kuai, J. Yang, J. Wang, Y. Nuli, Y. Guo and C. Liang, *Energy Storage Materials*, 2020, **33**, 452-459.
8. X. Cui, J. Yang, Z. Xu, Q. Liu, Y. Nuli and J. Wang, *Nano Energy*, 2022, **95**.
9. S. Liu, L. Deng, W. Guo, C. Zhang, X. Liu and J. Luo, *Adv. Mater.* , 2019, **31**, e1807585.
10. C. Wu, H. Huang, W. Lu, Z. Wei, X. Ni, F. Sun, P. Qing, Z. Liu, J. Ma, W. Wei, L. Chen, C. Yan and L. Mai, *Advanced Science*, 2020, **7**, 1902643.
11. L. Xie, Y. Deng, T. Wang, J. Deng, H. Ji, L. Wang, X. Niu and J. Gao, *J. Alloys Compd.*, 2022, **926**, 166437.